High-performance coherent population trapping clock with polarization modulation

Peter Yun[1],* François Tricot[1], Claudio Eligio Calosso[2], Salvatore Micalizio[2],
Bruno François[3], Rodolphe Boudot[3], Stéphane Guérandel[1], and Emeric de Clercq[1]

[1] *LNE-SYRTE, Observatoire de Paris, PSL Research University,*
CNRS, Sorbonne Universités, UPMC Univ. Paris 06,
61 avenue de l'Observatoire, 75014 Paris, France
[2] *Istituto Nazionale di Ricerca Metrologica, INRIM, Strada delle Cacce 91, 10135 Torino, Italy and*
[3] *FEMTO-ST, CNRS, UFC, 26 chemin de l'Épitaphe 25030 Besançon Cedex, France*
(Dated: October 4, 2016)

We demonstrate a vapor cell atomic clock prototype based on continuous-wave (CW) interrogation and double-modulation coherent population trapping (DM-CPT) technique. The DM-CPT technique uses a synchronous modulation of polarization and relative phase of a bi-chromatic laser beam in order to increase the number of atoms trapped in a dark state, *i.e.* a non-absorbing state. The narrow resonance, observed in transmission of a Cs vapor cell, is used as a narrow frequency discriminator in an atomic clock. A detailed characterization of the CPT resonance versus numerous parameters is reported. A short-term frequency stability of $3.2 \times 10^{-13} \tau^{-1/2}$ up to $100\,\mathrm{s}$ averaging time is measured. These performances are more than one order of magnitude better than industrial Rb clocks and comparable to those of best laboratory-prototype vapor cell clocks. The noise budget analysis shows that the short and mid-term frequency stability is mainly limited by the power fluctuations of the microwave used to generate the bi-chromatic laser. These preliminary results demonstrate that the DM-CPT technique is well-suited for the development of a high-performance atomic clock, with potential compact and robust setup due to its linear architecture. This clock could find future applications in industry, telecommunications, instrumentation or global navigation satellite systems.

I. INTRODUCTION

Microwave Rb vapor-cell atomic clocks [1], based on optical-microwave double resonance, are today ubiquitous timing devices used in numerous fields of industry including instrumentation, telecommunications or satellite-based navigation systems. Their success is explained by their ability to demonstrate excellent short-term fractional frequency stability at the level of $10^{-11} \tau^{-1/2}$, combined with a small size, weight, power consumption and a relatively modest cost. Over the last decade, the demonstration of advanced atom interrogation techniques (including for instance pulsed-optical-pumping (POP)) using narrow-linewidth semiconductor lasers has conducted to the development in laboratory of new-generation vapor cell clocks [2–5]. These clocks have succeeded to achieve a 100 times improvement in frequency stability compared to existing commercial vapor cell clocks.

In this domain, clocks based on a different phenomenon, named coherent population trapping (CPT), have proven to be promising alternative candidates. Since its discovery in 1976 [6], coherent population trapping physics [7–10] has motivated stimulating studies in various fields covering fundamental and applied physics such as slow-light experiments [11], high-resolution laser spectroscopy, magnetometers [12, 13], laser cooling [14] or atomic frequency standards. Basically, CPT occurs by connecting two long-lived ground state hyperfine levels of

an atomic specie to a common excited state by simultaneous action of two resonant optical fields. At null Raman detuning, i.e. when the frequency difference between both optical fields matches perfectly the atomic ground-state hyperfine frequency, atoms are trapped through a destructive quantum interference process into a noninteracting coherent superposition of both ground states, so-called dark state, resulting in a clear decrease of the light absorption or equivalently in a net increase of the transmitted light. The output resonance signal, whose line-width is ultimately limited by the CPT coherence lifetime, can then be used as a narrow frequency discriminator towards the development of an atomic frequency standard. In a CPT-based clock, unlike the traditional double-resonance Rb clock [15], the microwave signal used to probe the hyperfine frequency is directly optically carried allowing to remove the microwave cavity and potentially to shrink significantly the clock dimensions.

The application of CPT to atomic clocks was firstly demonstrated in a sodium atomic beam [16, 17]. In 1993, N. Cyr et al proposed a simple method to produce a microwave clock transition in a vapor cell with purely optical means by using a modulated diode laser [18], demonstrating its high-potential for compactness. In 2001, a first remarkably compact atomic clock prototype was demonstrated in NIST [19, 20]. Further integration was achieved later thanks to the proposal [21] and development of micro-fabricated alkali vapor cells [22], leading to the demonstration of the first chip-scale atomic clock prototype (CSAC) [23] and later to the first commercially-available CSAC [24]. Nevertheless, this extreme miniaturization effort induces a typical fractional

frequency stability limited at the level of $10^{-10}\tau^{-1/2}$, not compliant with dedicated domains requiring better stability performances. In that sense, in the frame of the European collaborative MClocks project [25], significant efforts have been pursued to demonstrate compact high-performance CPT-based atomic clocks and to help to push this technology to industry.

In standard CPT clocks, a major limitation to reach better frequency stability performances is the low contrast (C, the amplitude-to-background ratio) of the detected CPT resonance. This low contrast is explained by the fact that atoms interact with a circularly polarized bichromatic laser beam, leading most of the atomic population into extreme Zeeman sub-levels of the ground state, so called "end-states". Several optimized CPT pumping schemes, aiming to maximize the number of atoms participating to the clock transition, have been proposed in the literature to circumvent this issue ([26, 27], and references therein), but at the expense of increased complexity.

In that sense, a novel constructive polarization modulation CPT [28] pumping technique, named double-modulation (DM) scheme, was recently proposed. It consists to apply a phase modulation between both optical components of the bichromatic laser synchronously with a polarization modulation. The phase modulation is needed to ensure a common dark state to both polarizations, allowing to pump a maximum number of atoms into the desired magnetic-field insensitive clock state. This elegant solution presents the main advantage compared to the push-pull optical pumping [29–31] or the lin⊥lin technique [32, 33] to avoid any optical beam separation or superposition and is consequently well-adapted to provide a compact and robust linear architecture setup.

In this article, we demonstrate a high-performance CW-regime CPT clock based on the DM technique. Optimization of the short-term frequency stability is performed by careful characterization of the CPT resonance versus relevant experimental parameters. A short-term frequency stability at the level of $3.2 \times 10^{-13}\tau^{-1/2}$ up to 100 s, comparable to best vapor cell frequency standards, is reported. A detailed noise budget is given, highlighting a dominant contribution of the microwave power fluctuations. Section II describes the experimental setup. Section III reports the detailed CPT resonance spectroscopy versus experimental parameters. Section IV reports best short-term frequency stability results. Noise sources limiting the stability are carefully analysed. In section V, we study the clock frequency shift versus each parameter and estimate the limitation of the clock mid-term frequency stability.

II. EXPERIMENTAL SET-UP

A. Optical set-up

Our setup is depicted in Fig. 1. A DFB laser diode emits a monochromatic laser beam around 895 nm, the wavelength of the Cs D_1 line. With the help of a fiber electro-optic phase modulator (EOPM), modulated at 4.6 GHz with about 26 dBm microwave power, about 70% of the carrier power is transferred into both first-order sidebands used for CPT interaction. The phase between both optical sidebands, so-called Raman phase in the following, is further modulated through the driving 4.6 GHz microwave signal. Two acousto-optic modulators (AOMs) are employed. The first one, AOM1, is used for laser power stabilization. The second one, AOM2, allows to compensate for the buffer-gas induced optical frequency shift (≈ 160 MHz) in the CPT clock cell. A double-modulated laser beam is obtained by combining the phase modulation with a synchronized polarization modulation performed thanks to a liquid crystal polarization rotator (LCPR). The laser beam is expanded to $9\,\text{mm} \times 16\,\text{mm}$ before the vapor cell. The cylindrical Cs vapor cell, 25 mm diameter and 50 mm long, is filled with 15 Torr of mixed buffer gases (argon and nitrogen). Unless otherwise specified, the cell temperature is stabilized to about 35 °C. A uniform magnetic field of 3.43 µT is applied along the direction of the cell axis by means of a solenoid. The ensemble is surrounded by two magnetic shields in order to remove the Zeeman degeneracy.
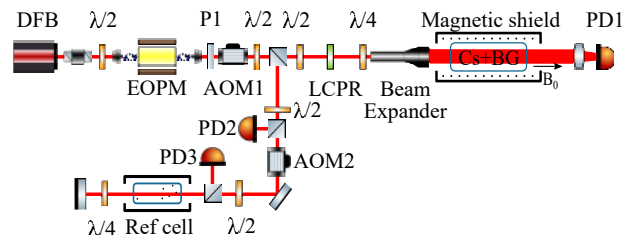

FIG. 1. (Color online) Optical setup for DM CPT, where the abbreviations stand for: DFB distributed feedback diode laser, EOPM electro-optic phase modulator, LCPR liquid crystal polarization rotator, AOM acousto-optic modulator, P polarizer, $\lambda/2(4)$ half(quarter)-wave plate, BG buffer gas, PD photodiode.

B. Fiber EOPM sidebands generation

We first utilized a Fabry-Perot cavity to investigate the EOPM sidebands power ratio versus the coupling 4.596 GHz microwave power ($P_{\mu w}$), see Fig. 2. We choose $P_{\mu w}$ around 26 dBm to maximize the power transfer efficiency into the first-order sidebands. The sidebands spectrum is depicted in the inset of Fig. 2.
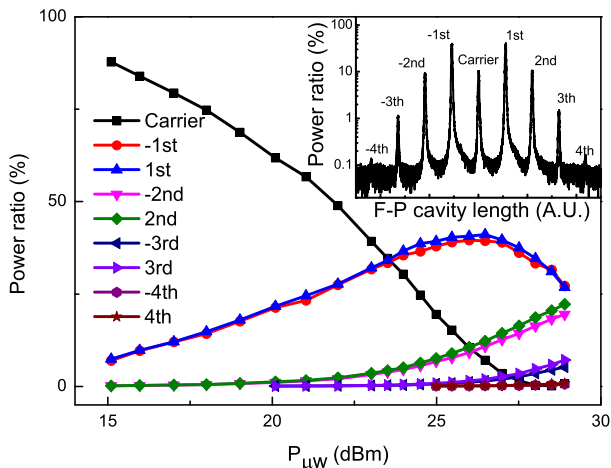
FIG. 2. (Color online) Fractional power of laser sidebands at the EOPM output as a function of 4.596 GHz microwave power. Inset, the laser sidebands spectrum with $P_{\mu w} = 26.12$ dBm obtained by scanning the FP cavity length, notice the log scale of the y-axis.
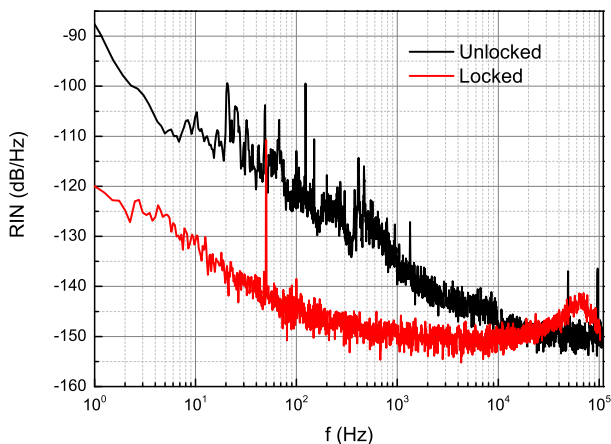
C. Laser power locking

FIG. 3. (Color online)Power spectral density of the laser RIN with and w/o power locking.

Since the laser intensity noise is known as being one of the main noise sources which limit the performances of a CPT clock [10, 31], laser power needs to be carefully stabilized. For this purpose, a polarization beam splitter (PBS) reflects towards a photo-detector a part of the laser beam, the first-order diffracted by AOM1 following the EOPM. The output voltage signal is compared to an ultra-stable voltage reference (LT1021). The correction signal is applied on a voltage variable power attenuator set on the feeding RF power line of the AOM1 with a servo bandwidth of about 70 kHz. The out-loop laser intensity noise (RIN) is measured just after the first PBS with a photo-detector (PD), which is not shown in Fig. 1. The spectrum of the resulting RIN with and

w/o locking is shown in Fig. 3. A 20 dB improvement at $F_M = 125$ Hz (LO modulation frequency for clock operation) is obtained in the stabilized regime.

It is worth to note that the DFB laser diode we used, with a linewidth of about 2 MHz, is sensitive even to the lowest levels of back-reflections [34], e.g., the coated collimated lens may introduce some intensity and frequency noise at the regime of 0.1 kHz to 10 kHz. Finding the correct lens alignment to minimize the reflection induced noise while keeping a well-collimated laser beam was not an easy task. To reduce light feedback from the EOPM fiber face, we use a 60 dB isolator before the EOPM. The fiber-coupled EOPM induces additional intensity noise depicted in Fig. 3. Nevertheless, thanks to the laser power locking, we can reduce most of these noises by at least 15 dB in the range of 1 Hz to 1 kHz.

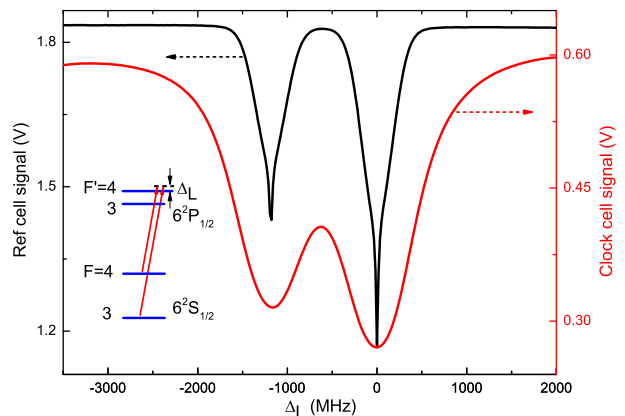### D. Laser frequency stabilization

FIG. 4. (Color online) Spectrum of the Cs D_1 line in the vacuum reference cell and in the clock cell recorded with the bichromatic laser. The two absorptions from left to right correspond to the excited level $|6^2P_{1/2}, F' = 3\rangle$ and $|6^2P_{1/2}, F' = 4\rangle$, respectively. For the reference cell signal: laser power 0.74 mW, beam diameter 2 mm, cell temperature 22 °C, AOM frequency 160 MHz. Inset, the atomic levels involved in D_1 line of Cesium.

Our laser frequency stabilization setup, similar to [31, 35], is depicted in Fig. 1. We observe in a vacuum cesium cell the two-color Doppler-free spectrum depicted in Fig. 4. The bi-chromatic beam, linearly polarized, is retro-reflected after crossing the cell with the orthogonal polarization. Only atoms of null axial velocity are resonant with both beams. Consequently, CPT states built by a beam are destroyed by the reversed beam, leading to a Doppler-free enhancement of the absorption [35].

The laser frequency detuning $\Delta_L = 0$ in Fig. 4 corresponds to the laser carrier frequency tuned to the center of both transitions $|6^2S_{1/2}, F = 3\rangle \rightarrow |6^2P_{1/2}, F' = 4\rangle$ and $|6^2S_{1/2}, F = 4\rangle \rightarrow |6^2P_{1/2}, F' = 4\rangle$ in D_1 line of Cesium, where F is the hyperfine quantum number. For
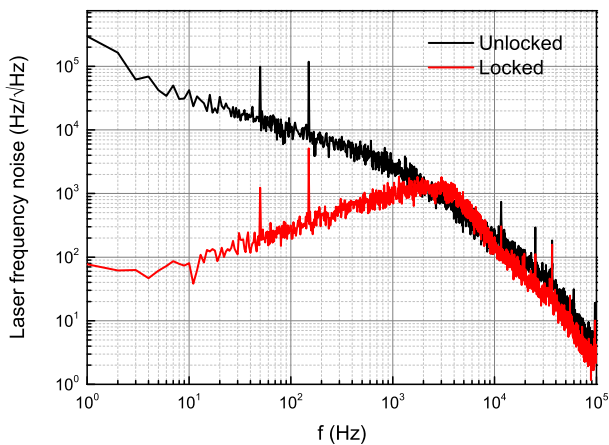
FIG. 5. (Color online) The laser frequency noise measured on the error signal of the Doppler-free spectrum with and w/o frequency locking.

this record, the microwave frequency is 4.596 GHz, half the Cs ground state splitting, and the DFB laser frequency is scanned. The frequency noise with and w/o locking are presented in Fig. 5. The servo bandwidth is about 3 kHz and the noise is found to be reduced by about 25 dB at $f = 125$ Hz (local oscillator modulation frequency in clock operation).

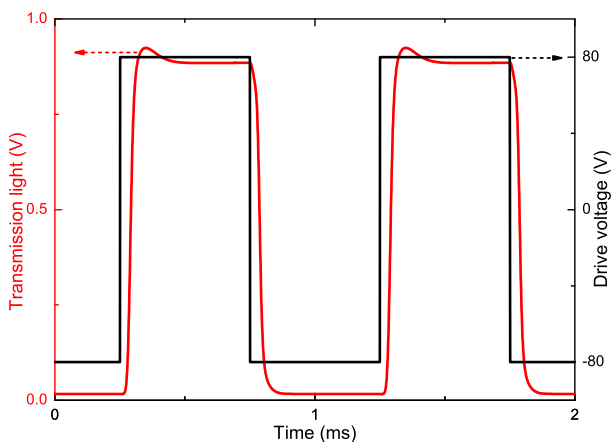## E. Polarization modulation

FIG. 6. (Color online) LCPR response.

We studied the response time of the LCPR (FPR-100-895, Meadowlark Optics). As illustrated in Fig. 6, the measured rise (fall) time is about 100 μs and the polarization extinction ratio is about 50. In comparison, the electro-optic amplitude modulator (EOAM) used as polarization modulator in our previous investigations [28] showed a response time of 2.5 μs (limited by our high voltage amplifier) and a polarization extinction ratio of 63. Here, we replace it by a liquid crystal device because

its low voltage and small size would be an ideal choice for a compact CPT clock, and we will show in the following that the longer switching time does not limit the contrast of the CPT signal.
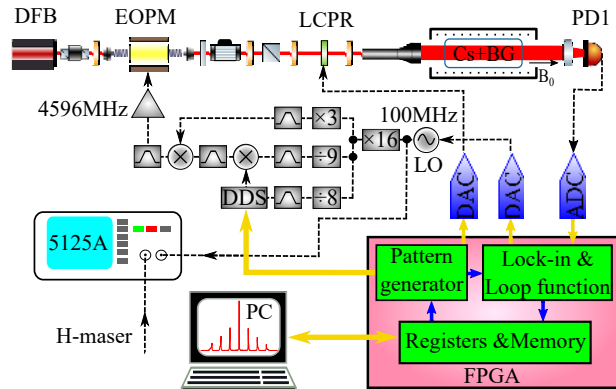
F. Microwave source and clock servo-loop

FIG. 7. (Color online) Electronic architecture of the DM CPT clock: DDS direct digital synthesizer, DAC digital-to-analog converter, ADC analog-to-digital converter, FPGA field programmable gate array, LO local oscillator.

The electronic system (local oscillator and digital electronics for clock operation) used in our experiment is depicted in Fig. 7. The 4.596 GHz microwave source is based on the design described in [36]. The local oscillator (LO) is a module (XM16 Pascall) integrating an ultra-low phase noise 100 MHz quartz oscillator frequency-multiplied without excess noise to 1.6 GHz. The 4.596 GHz signal is synthesized by a few frequency multiplication, division and mixing stages. The frequency modulation and tuning is yielded by a direct digital synthesizer (DDS) referenced to the LO. The clock operation [2, 37] is performed by a single field programmable gate array (FPGA) which coordinates the operation of the DDS, analog-to-digital converters (ADC) and digital-to-analog converter (DACs):

(1) the DDS generates a signal with phase modulation (modulation rate f_m, depth $\pi/2$) and frequency modulation (F_M, depth Δ_{F_M}).

(2) the DAC generates a square-wave signal to drive the LCPR with the same rate f_m, synchronous to the phase modulation.

(3) the ADC is the front-end of the lock-in amplifier. Another DAC, used to provide the feedback to the local oscillator frequency, is also implemented in the FPGA.

The clock frequency is measured by comparing the LO signal with a 100 MHz signal delivered by a H maser of the laboratory in a Symmetricom 5125A Allan deviation test set. The frequency stability of the maser is 1×10^{-13} at 1 s integration time.

III.   CLOCK SIGNAL OPTIMIZATION

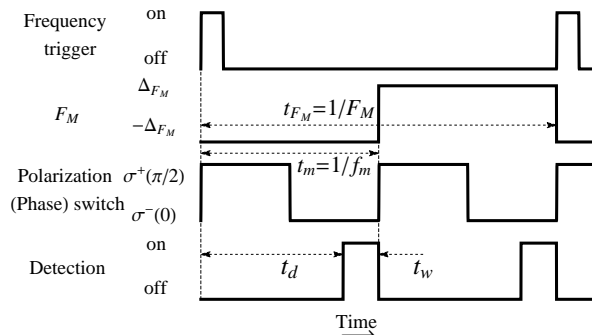### A.   Time sequence and figure of merit

FIG. 8.   Time sequence. F_M modulation frequency of the 4.596 GHz signal, f_m polarization and phase modulation frequency, t_d pumping time, t_w detection window.

As illustrated in Fig. 8, the polarization and phase modulation share the same modulation function. After a pumping time t_d to prepare the atoms into the CPT state, we detect the CPT signal with a window of length t_w. In order to get an error signal to close the clock frequency loop, the microwave frequency is square-wave modulated with a frequency F_M, and a depth Δ_{F_M}. In our case, we choose $F_M = 125$ Hz, as a trade-off between a low frequency to have time to accumulate the atomic population into the clock states by the DM scheme and a high operating frequency to avoid low frequency noise in the lock-in amplification process and diminish the intermodulation effects.
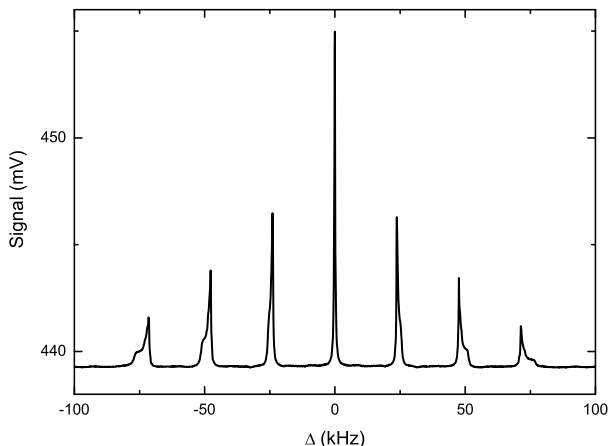

FIG. 9. Zeeman spectrum. The center peak is the $0-0$ clock transition. Working parameters: $t_d = 2$ ms, $t_w = 2$ ms, $f_m = 500$ Hz, $P_L = 163\,\mu\text{W}$, $P_{\mu w} = 26.12$ dBm, $T_{cell} = 35.1\,^\circ$C.

A typical experimental CPT signal, recorded with this time sequence, showing all the CPT transitions allowed between Zeeman sub-levels of the Cs ground state is reported in Fig. 9. The Raman detuning Δ is the difference between the two first sideband spacing and the Cs clock resonance. The spectrum shows that the clock levels ($0-0$ transition) are the most populated and that the atomic population is symmetrically distributed around the ($m = 0$) sub-levels. The distortion of neighbouring lines is explained by magnetic field inhomogeneities.

It can be shown that the clock short-term frequency stability limited by an amplitude noise scales as W_h/C [10], with W_h the full width at half maximum (FWHM) of the clock resonance, and C the contrast of the resonance. Usually, the ratio of contrast C to W_h is adopted as a figure of merit, i.e. $F_C = C/W_h$. The best stability should be obtained by maximizing F_C.

The stability of the clock is measured by the Allan standard deviation $\sigma_y(\tau)$, with τ the averaging time. When the signal noise is white, with standard deviation σ_N, and for a square-wave frequency modulation, the stability limited by the signal-to-noise ratio is equal to [38]

$$\sigma_y(\tau) = \frac{1}{f_c}\frac{\sigma_N}{S_\ell}\sqrt{\frac{1}{\tau}}, \tag{1}$$

with f_c the clock frequency, and S_ℓ the slope of the frequency discriminator. In CPT clocks, one of the main sources of noise is the laser intensity noise, which leads to a signal noise proportional to the signal. Therefore it is more convenient to characterize the quality of the signal of a CPT atomic clock by a new figure of merit, $F_S = S_\ell/V_{wp}$, where S_ℓ is the slope of the error signal (in V/Hz) at Raman resonance ($\Delta = 0$), and V_{wp} is the detected signal value (in V) at the interrogating frequency (the clock resonance frequency plus the modulation depth Δ_{F_M}), see Fig. 10. Note that an estimation of the discriminator slope is also included in F_C, since the contrast is the signal amplitude A divided by the background B. F_C then equals $(A/W_h)/B$, (A/W_h) is a rough approximation of the slope S_ℓ, and B an approximation of the working signal V_{wp}. In our experimental conditions $A/W_h \sim S_\ell/3$.

We investigated the effect of relevant parameters on both figures of merit to optimize the clock performances. In order to allow a comparison despite different conditions, the error signals are generated with the same unit gain. Since the resonance linewidth is also subject to change, it is necessary to optimize the 4.6 GHz modulation depth Δ_{F_M} to maximize F_S. Here for simplicity, we first recorded the CPT signal, then we can numerically compute optimized values of Δ_{F_M} and F_S.

In the following, we investigate the dependence of F_C and F_S on several parameters including the cell temperature (T_{cell}), the laser power (P_L), the microwave power ($P_{\mu w}$), the detection window duration (t_w), the detection start time (t_d), and the polarization and phase modulation frequency (f_m).
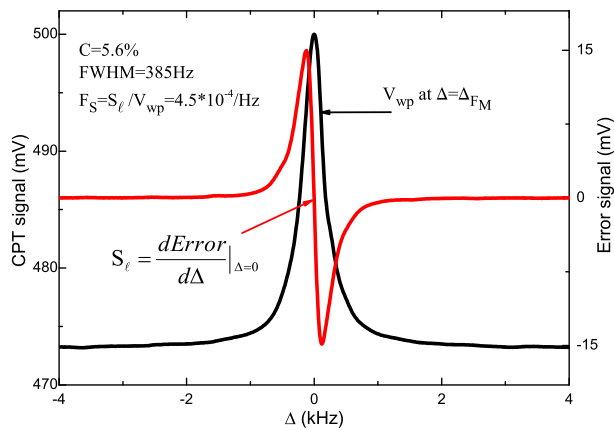
FIG. 10. (Color online) Signal of the clock transition and error signal. Working parameters: $t_d = 3\,\text{ms}$, $t_w = 1\,\text{ms}$, $f_m = 250\,\text{Hz}$, $P_L = 163\,\mu\text{W}$, $P_{\mu w} = 26.12\,\text{dBm}$, $T_{cell} = 35.1\,°\text{C}$.

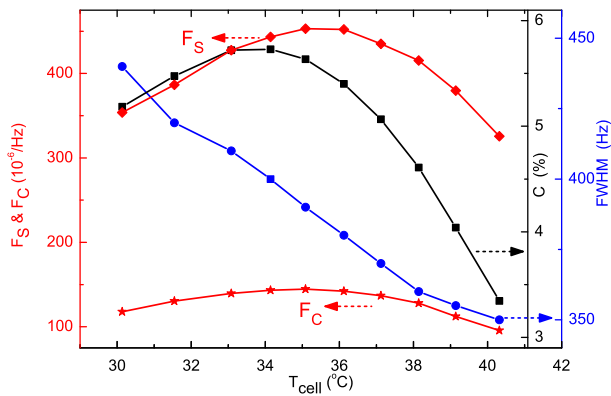### B. Cell temperature and laser power

FIG. 11. (Color online) Figures of merit F_S, F_C, contrast C and width of the clock transition as function of cell temperature T_{cell}. All other working parameters is the same as Fig. 10.

From the figures of merit shown in Fig. 11, the optimized cell temperature is around $T_{cell} = 35.1\,°\text{C}$ for $P_L = 163\,\mu\text{W}$. The narrower linewidth observed at higher T_{cell}, already observed by Godone $et\ al.$ [39], can be explained by the propagation effect: the higher the cell temperature, the stronger the light absorption by more atoms, and less light intensity is seen by the atoms at the end side of the vapour cell. This leads to a reduction of the power broadening and a narrower signal, measured by the transmitted light amplitude. The optimum temperature depends on the laser power as depicted in Fig. 12. Nevertheless, the overall maximum of F_S is reached with $P_L = 163\,\mu\text{W}$ at $T_{cell} = 35.1\,°\text{C}$.

The figures of merit F_S, F_C, the contrast C and the width are plotted as a function of the laser power in Fig. 13 for $T_{cell} = 35.1\,°\text{C}$. The laser powers maximizing F_S and F_C are $P_L = 163\,\mu\text{W}$ and $P_L = 227\,\mu\text{W}$, re-
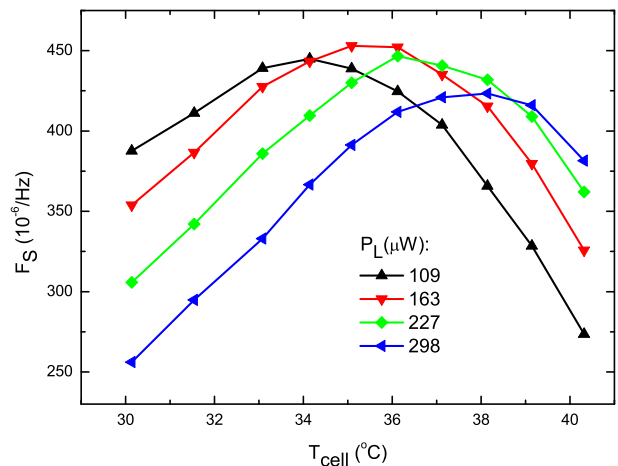

FIG. 12. (Color online) F_S as a function of cell temperature T_{cell} for various laser powers. All other working parameters is the same as Fig. 10.

spectively. The Allan deviation reaches a better value at $P_L = 163\,\mu\text{W}$, which justifies our choice of F_S as figure of merit. And in the following parameters investigation, we only show the F_S as figure of merit for clarity.
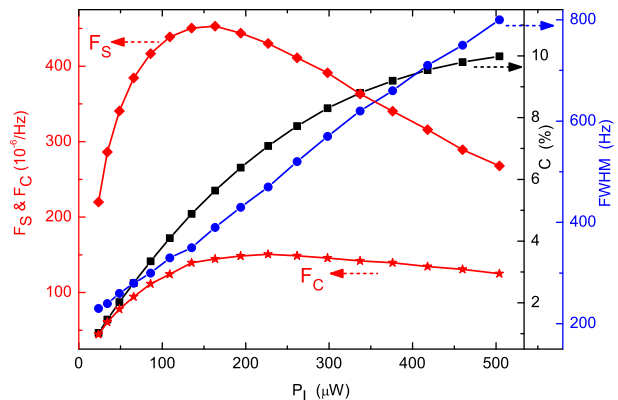

FIG. 13. (Color online) F_S, F_C, C and width of the clock transition as a function of laser power P_L with $T_{cell} = 35.1\,°\text{C}$. All other working parameters is the same as Fig. 10.

C. Microwave power

F_S, C and width versus the microwave power are shown in Fig. 14. The behaviour of F_S is basically in agreement with the fractional power of first (±1) sidebands of Fig. 2. The optimized microwave power is around $26.12\,\text{dBm}$.
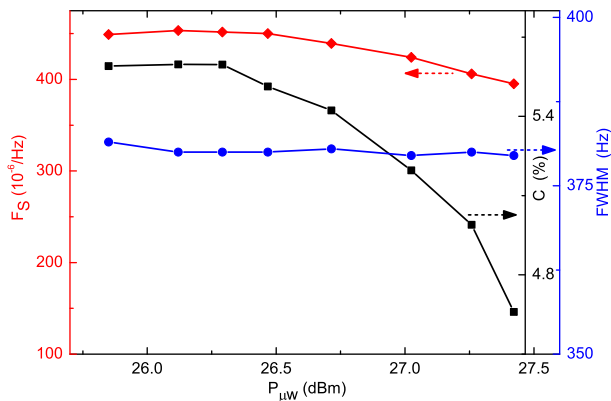
FIG. 14. (Color online) F_S, C and width of the clock transition as function of microwave power $P_{\mu w}$ with $T_{cell} = 35.1\,°C$. All other working parameters is the same as Fig. 10.

D. Detection window t_w and pumping time t_d

As we can see on Fig. 15, a short detection window t_w would generate a higher contrast signal and higher figures of merit. However, we found that a longer time, e.g., $t_w = 1\,ms$, results in a better Allan deviation at one-second averaging time. It is due to the conflict between the higher signal slope ($\propto F_S$) and the increased number of detected samples which help to reduce the noise, see Eq.(5).
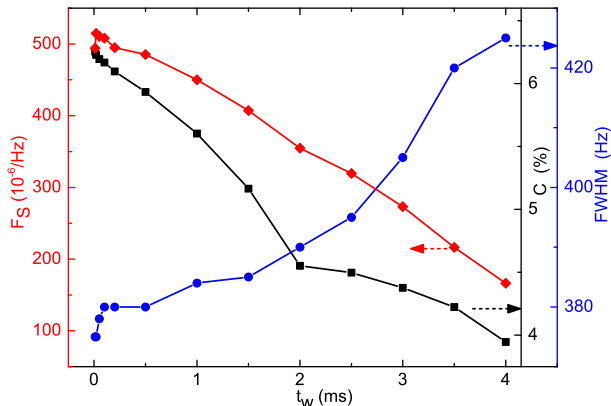

FIG. 15. (Color online) F_S, C and width of the clock transition as a function of t_w. With $t_d = 4\,ms - t_w$ and all other working parameters is the same as Fig. 10.

The same parameters are plotted versus the pumping time t_d in Fig. 16. The figures of merit and C firstly increase and then decrease at $t_d = 1\,ms$, because when the detection window $t_w \geq 1\,ms$, the signals of two successive polarizations are included. The dynamic behaviour of the atomic system induces the decrease of the CPT amplitude (see Fig. 10 in [40]). After $t_d = 2\,ms$, F_S increases again and reach a maximum. Thus we can say that, in a certain range, a longer t_d will lead to a greater atomic population pumped into the clock states as de-

picted in Fig. 16, yielding higher figures of merit. The behaviour of the linewidth versus the pumping time is not explained to date. Nevertheless, note that here the steady-state is not reached and the width behaviour results certainly from a transient effect.
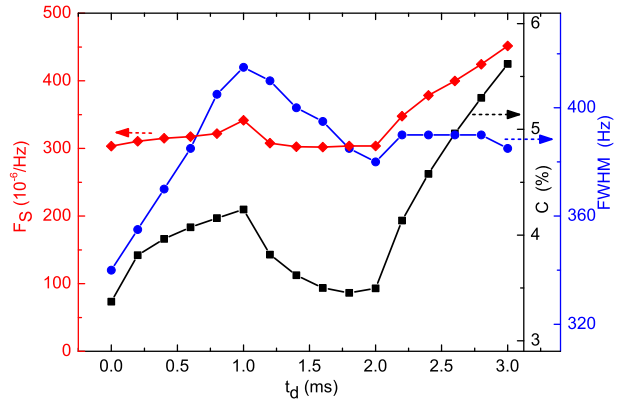

FIG. 16. (Color online) F_S, C and width of the clock transition versus t_d. All other working parameters is the same as Fig. 10.

E. Polarization-and-phase modulation frequency f_m

Figure 17 shows F_S, C, and width versus the polarization (and phase) modulation frequency f_m The maxima of F_S is reached at low frequency f_m. In one hand, this is an encouraging result to demonstrate the suitability of the LCPR polarization modulator in this experiment. In an other hand, the higher F_M rate would be better for a clock operation with lock-in method to modulate and demodulate the error signal, to avoid the low frequency noises such as $1/f$ noise. Therefore, we chose $F_M = 125\,Hz$ and $f_m = 250\,Hz$. We have noticed that the behavior of C is not exactly the same than the one observed in our previous work [40, 41] with a fast EOAM, where the signal amplitude was maximized at higher frequencies. This can be explained by the slower response time of the polarization modulator and the lower laser intensity used. The linewidth reaches a minimum around $1.5\,kHz$. This behaviour will be investigated in the future.

IV. FREQUENCY STABILITY

A. Measured stability

The high contrast and narrow line-width CPT signal obtained with the optimized values of the parameters is presented in Fig. 10, with the related error signal. The Allan standard deviation of the free-running LO and of the clock frequency, measured against the H maser, are shown in Fig. 18. The former is in correct
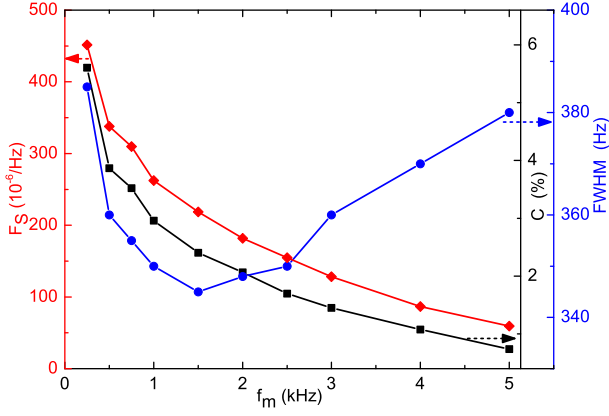
FIG. 17. (Color online) The F_S, C and width of the clock transition as function of f_m. All other working parameters is the same as Fig. 10.

agreement with its measured phase noise. In the $1\,\mathrm{Hz}$ to $100\,\mathrm{Hz}$ offset frequency region, the phase noise spectrum of the free-running $4.596\,\mathrm{GHz}$ LO signal is given in $\mathrm{dBrad^2/Hz}$ by $S_\varphi(f) = b_{-3}f^{-3}$ with $b_{-3} = -47$, signature of a flicker frequency noise [36]. This phase noise yields an expected Allan deviation given by $\sigma_y(1\,\mathrm{s}) \approx \sqrt{2\ln 2 \times \frac{4b_{-3}}{f_c^2}} \approx 1.2 \times 10^{-12}$ [42], close to the measured value of 2×10^{-12} at $1\,\mathrm{s}$. The measured stability of the CPT clock is $3.2 \times 10^{-13}\tau^{-1/2}$ up to $100\,\mathrm{s}$ averaging time for our best record. This value is close to the best CPT clocks [31, 33], demonstrating that a high-performance CPT clock can be built with the DM-CPT scheme. A typical record for longer averaging times is also shown in Fig. 18. For averaging times τ longer than $20\,\mathrm{s}$, the Allan deviation increases like $\sqrt{\tau}$, signature of a random walk frequency noise.
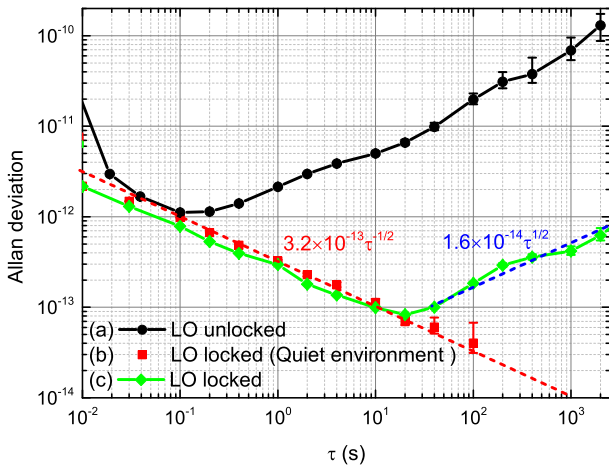

FIG. 18. (Color online) The LO frequency stability (a) free running, (b) and (c) locked on the atomic resonance. (b) best record in quiet environment, (c) typical record. The slope of the red (blue) dashed fitted line is $3.2 \times 10^{-13}\tau^{-1/2}$ ($1.6 \times 10^{-14}\tau^{1/2}$), respectively.

B.   Short-term stability limitations

We have investigated the main noise sources that limit the short-term stability. For a first estimation, we consider only white noise sources, and for the sake of simplicity we assume that the different contributions can independently add, so that the total Allan variance can be computed as

$$\sigma_y^2(\tau) = \Sigma_i \sigma_{y,p_i}^2(\tau) + \sigma_{y,LO}^2(\tau), \qquad (2)$$

with $\sigma_{y,LO}^2(\tau)$ the contribution due to the phase noise of the local oscillator, and $\sigma_{y,p_i}^2(\tau)$ the Allan variance of the clock frequency induced by the fluctuations of the parameter p_i. When p_i modifies the clock frequency during the whole interrogation cycle, $\sigma_{y,p_i}^2(\tau)$ can be written

$$\sigma_{y,p_i}^2(\tau) = \frac{1}{f_c^2}\left(\sigma_{p_i}^2\right)_{1Hz}\left(\delta f_c/\delta p_i\right)^2 \frac{1}{\tau}, \qquad (3)$$

with $\left(\sigma_{p_i}^2\right)_{1Hz}$ the variance of p_i measured in 1 Hz bandwidth at the modulation frequency F_M, $\left(\delta f_c/\delta p_i\right)$ is the clock frequency sensitivity to a fluctuation of p_i. Here, the detection signal is sampled during a time window t_w with a sampling rate $2F_M = 1/T_c$, where T_c is a cycle time. In this case Eq.(3) becomes

$$\sigma_{y,p_i}^2(\tau) = \frac{1}{f_c^2}\left(\sigma_{p_i}^2\right)_{tw}\left(\delta f_c/\delta p_i\right)^2 \frac{T_c}{\tau}, \qquad (4)$$

with $\left(\sigma_{p_i}^2\right)_{tw}$ the variance of p_i sampled during t_w; $\left(\sigma_{p_i}^2\right)_{tw} \approx S_{p_i}(F_M)/(2t_w)$ with $S_{p_i}(F_M)$ the value of the power spectral density (PSD) of p_i at the Fourier frequency F_M (assuming a white frequency noise around F_M). When p_i induces an amplitude fluctuation with a sensitivity $\left(\delta V_{wp}/\delta p_i\right)$, Eq.(4) becomes

$$\sigma_{y,p_i}^2(\tau) = \frac{1}{f_c^2}S_{p_i}(F_M)\frac{\left(\delta V_{wp}/\delta p_i\right)^2}{S_\ell^2}\frac{T_c}{2t_w}\frac{1}{\tau}, \qquad (5)$$

with S_ℓ the slope of the frequency discriminator in V/Hz. We review below the contributions of the different sources of noise.

Detector noise: the square root of the power spectral density (PSD) S_d of the signal fluctuations measured in the dark is shown in Fig. 19. It is $N_{detector} = 64.8$ $\mathrm{nV}/\sqrt{\mathrm{Hz}}$ in 1 Hz bandwidth at the Fourier frequency $125\,\mathrm{Hz}$. According to Eq.(5) the contribution of the detector noise to the Allan deviation at one second is 0.45×10^{-13}.

Shot-noise: with the transimpedance gain $G_R = 1.5 \times 10^4\,\mathrm{V\,A^{-1}}$ and the detector current $I = V_{wp}/G_R = 32.7\,\mathrm{\mu A}$, Eq.(5) becomes

$$\sigma_{y,sh}^2(\tau) = \frac{1}{f_c^2}\frac{(2eIG_R)^2}{S_\ell^2}\frac{T_c}{2t_w}\frac{1}{\tau}, \qquad (6)$$
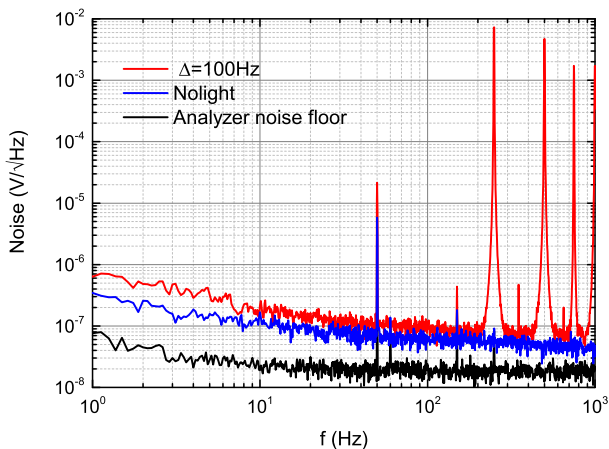
FIG. 19. (Color online) The RIN after the cell, detector noise and analyser noise floor. Working parameters is the same as Fig. 10.

with e the electron charge. The contribution to the Allan deviation at one second is 0.34×10^{-13}.

Laser FM-AM noise: it is the amplitude noise induced by the laser carrier frequency noise. The slope of the signal V_{wp} with respect to the laser frequency f_L is $S_{FM-AM} = 0.16\,\mathrm{mV\,MHz}^{-1}$ at optical resonance. According to Eq.(5) with data of laser-frequency-noise PSD of Fig. 5 at 125 Hz, we get a Allan deviation of 0.33×10^{-13} at one second.

Laser AM-AM noise: it is the amplitude noise induced by the laser intensity noise. The measured signal sensitivity to the laser power is $S_{AM} = 3.31\,\mathrm{mV\,\mu W}^{-1}$ at $f_L = 163\,\mu W$, combined with the laser intensity PSD of Fig. 3 it leads to the amplitude noise $S_{AM} \times P_L \times RIN(125\,\mathrm{Hz}) = 30.3\,\mathrm{nV}/\sqrt{\mathrm{Hz}}$, and an Allan deviation of 0.21×10^{-13} at one second.

LO phase noise: the phase noise of the local oscillator degrades the short-term frequency stability via the intermodulation effect [43]. It can be estimated by:

$$\sigma_{y_{LO}}(1s) \sim \frac{F_M}{f_c}\sqrt{S_\varphi(2F_M)}. \qquad (7)$$

Our $4.596\,\mathrm{GHz}$ microwave source is based on [36] which shows an ultra-low phase noise $S_\varphi(2F_M) = -116\,\mathrm{dB\,rad^2\,Hz^{-1}}$ at $2F_M = 250\,\mathrm{Hz}$ Fourier frequency. This yields a contribution to the Allan deviation of 0.43×10^{-13} at one second.

Microwave power noise: fluctuations of microwave power lead to a laser intensity noise, which is already taken into account in the RIN measurement. We show in the next section that they also lead to a frequency shift (see Fig. 22). The Allan deviation of the microwave power at 1 s is $2.7 \times 10^{-4}\,\mathrm{dBm}$, see inset of Fig. 22. With a measured slope of 7.7 Hz/dBm, we get a fractional-frequency Allan deviation of 2.26×10^{-13}, which is the largest contribution to the stability at 1 s. Note that in our set-up the microwave power is not stabilized.

The other noise sources considered have much lower contributions, they are the laser frequency-shift effect, *i.e.* AM-FM and FM-FM contributions, the cell temperature and the magnetic field. Table I resumes the short-term stability noise budget.

TABLE I. Noise contributions to the stability at 1 s.

Noise source	noise level	$\sigma_y(1s) \times 10^{13}$
Detector noise	$64.8\,\mathrm{nV}/\sqrt{\mathrm{Hz}}$	0.45
Shot noise	$48.8\,\mathrm{nV}/\sqrt{\mathrm{Hz}}$	0.34
Laser FM-AM	$48.0\,\mathrm{nV}/\sqrt{\mathrm{Hz}}$	0.33
Laser AM-AM	$30.3\,\mathrm{nV}/\sqrt{\mathrm{Hz}}$	0.21
LO phase noise	$-116\,\mathrm{dBrad^2/Hz}$	0.43
$P_{\mu w}$	$2.7 \times 10^{-4}\,\mathrm{dBm@1\,s}$	2.26
Laser AM-FM	$0.6\,\mathrm{nW@1\,s}$	9.7×10^{-3}
Laser FM-FM	$\sim 100\,\mathrm{Hz@1\,s}$	2.9×10^{-3}
T_{cell}	$6.3 \times 10^{-5}\,\mathrm{K@1\,s}$	3.2×10^{-2}
B_0	$4.3\,\mathrm{pT@1\,s}$	1.4×10^{-3}
Total		2.4

The laser intensity noise after interacting with the atomic vapor is depicted in Fig. 19. It encloses the different contributions to the amplitude noise, *i.e.* detector noise, shot-noise, FM-AM and AM-AM noises. The noise spectral density is $100\,\mathrm{nV}/\sqrt{\mathrm{Hz}}$ at the Fourier frequency 125 Hz, which leads to an Allan deviation of 0.7×10^{-13} at 1 s. This value is equal to the quadratic sum of the individual contributions. The quadratic sum of all noise contribution leads to an Allan deviation at one second of 2.4×10^{-13}, while the measured stability is $3.2 \times 10^{-13}\tau^{-1/2}$ (Fig. 18). The discrepancy could be explained by correlations between different noises, which are not all independent. The dominant contribution is the clock frequency shift induced by the microwave power fluctuations. This term could be reduced by microwave power stabilization or a well chosen laser power (see Fig. 14), but to the detriment of the signal amplitude.

V. FREQUENCY SHIFTS AND MID-TERM STABILITY

We have investigated the clock-frequency shift with respect to the variation of various parameters. For each frequency measurement, the LO frequency is locked on the CPT resonance. With a 100 s averaging time, the mean frequency is measured with typical error bar less than 10^{-12}, *i.e.*, 0.01 Hz relative to the Cs frequency $f_{Cs} = 9.192\,\mathrm{GHz}$.

A. f_0 vs T_{cell}

The resonance frequency of the microwave resonance is shifted by collisions between Cs atoms and buffer-gas atoms [38]. This collisional shift is temperature dependent but can be reduced by using a well-chosen mixture of gas. Here we use a N_2-Ar mixture with 37% of Ar, optimized for cancelling the temperature coefficient at $31.5\,°C$ and which should allow to reduce the sensitivity of the cock frequency at the level of $-0.16\,Hz\,K^{-1}$ at $35\,°C$ [44]. The record of the frequency shift versus T_{cell} is presented in Fig. 20. The temperature sensitivity is measured to be $0.47\,Hz\,K^{-1}$ at $T_{cell} = 35\,°C$. This value is in disagreement with the expected value. Nevertheless, it is important to note that the latter is valid at null laser power and that the laser power shift is also temperature-dependent [45]. In this experimental test, we measure the result of the collisional shift and of the laser power shift together. The Allan deviation of T_{cell} is shown in the inset of Fig. 20. With a typical temperature fluctuation of $5.2 \times 10^{-5}K$ at $1000\,s$, the contribution of cell temperature variations to the clock fractional frequency stability is about 2.7×10^{-15} at $1000\,s$.
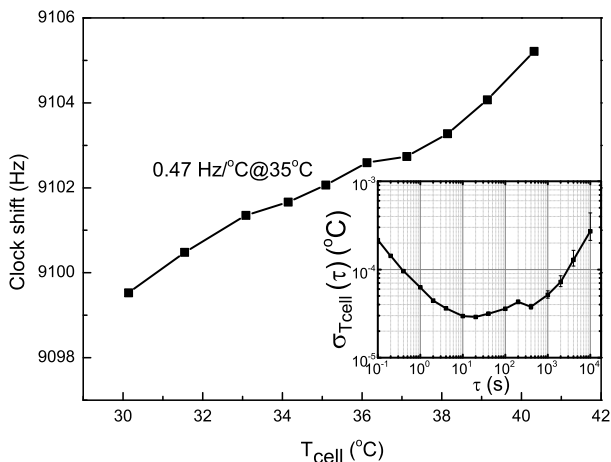

FIG. 20. (Color online) Clock frequency as a function of the cell temperature T_{cell}. The inset shows the Allan deviation of T_{cell}. All other working parameters is the same as Fig. 10.

B. f_0 vs P_L

The clock frequency shift versus P_L is presented in Fig. 21. The coefficient of the light power shift is $14.9\,Hz\,mW^{-1}$ at $P_L = 163\,\mu W$ and $P_{\mu w} = 26.12\,dBm$. This shift is difficult to foresee theoretically because it results of the combination of light shifts (AC Stark shift) induced by all sidebands of the optical spectrum, but also of overlapping and broadening of neighboring lines. The inset of Fig. 21 shows the typical fractional fluctuations the laser power versus the integration time. They are measured to be 1×10^{-4} at 1000 s, impacting on the clock

fractional frequency stability at the level of 2.6×10^{-14} at $1000\,s$. Since the power distribution in the sidebands vary with the microwave power, the laser power shift is also sensitive to the microwave power feeding the EOPM. This is clearly shown in Fig. 21. As previously observed in CPT-based clocks [46, 47] and double-resonance Rb clocks [48], it is important to note that the light-power shift coefficient can be decreased and even cancelled at specific values of $P_{\mu w}$. Consequently, it should be possible to improve the long-term frequency stability by tuning finely the microwave power value [49, 50], at the expense of a slight degradation of the short-term frequency stability.
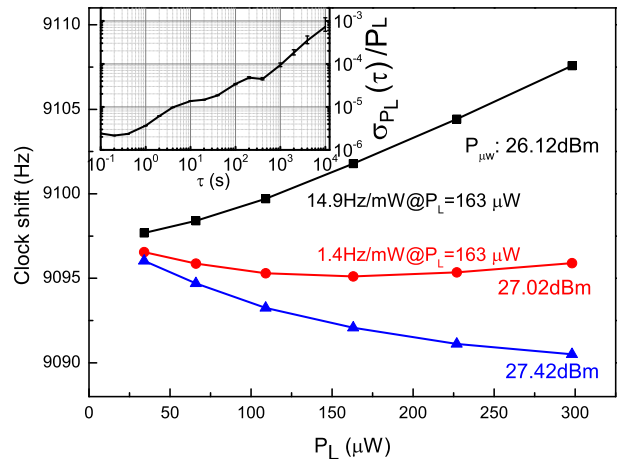

FIG. 21. (Color online) Clock frequency as a function of laser power P_L for different values of $P_{\mu w}$. Inset: fractional Allan deviation of the laser power. All other working parameters is the same as Fig. 10.

C. f_0 vs $P_{\mu W}$

The frequency shift versus the microwave power at fixed laser power is shown on Fig. 22. At constant optical power, only the power distribution among the different sidebands changes. This is a different laser power effect. The shift scales as the microwave power in the investigated range, with a sensitivity of $7.7\,Hz\,dBm^{-1}$ at $P_L = 163\,\mu W$. In this range, the power ratio of both first (± 1) sidebands changes by about 10%. The inset of Fig. 22 shows the Allan deviation of the microwave power in dBm. The typical microwave power standard deviation of $5 \times 10^{-4}\,dBm$ at $1000\,s$ yields a fractional frequency stability of about 4.2×10^{-13} at $1000\,s$.

D. f_0 vs Δ_L

The frequency of the laser beam incident on the clock cell can be tuned by setting the driving frequency of AOM2 in the laser frequency stabilization setup. For
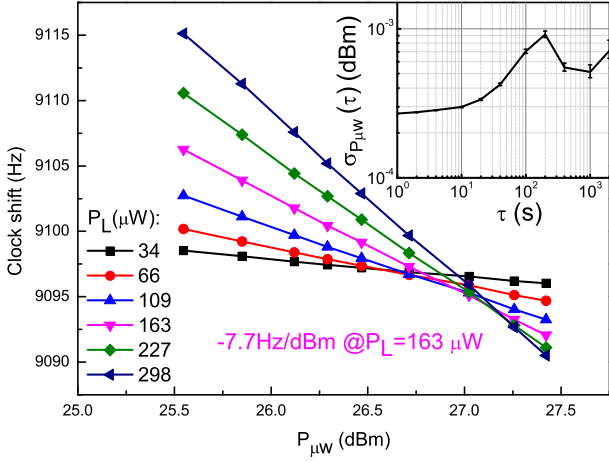
FIG. 22. (Color online) Clock frequency as a function of the microwave power $P_{\mu w}$. Inset: Allan deviation of the microwave power in dBm, log scale. All other working parameters is the same as Fig. 10.
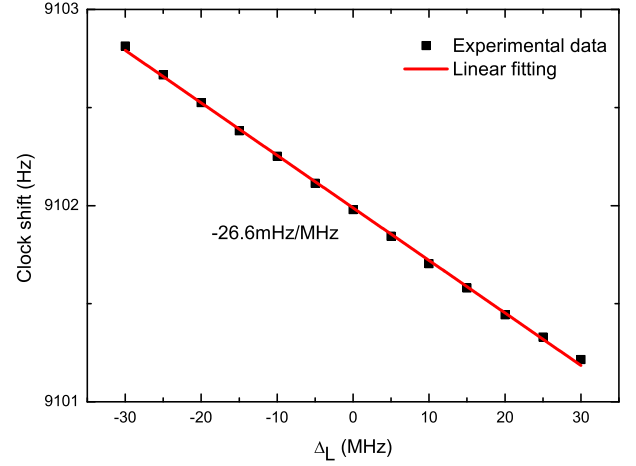

FIG. 23. (Color online) Clock frequency as a function of laser frequency detuning Δ_L. Experimental data are fitted by a linear function. All other working parameters is the same as Fig. 10.

each AOM driving frequency, the laser carrier frequency is stabilized onto the reference cell, the clock frequency is locked onto the CPT resonance and measured against the hydrogen maser. The observed shift results from a combination of AC Stark shift, CPT resonance distortion and effect of neighboring lines. The recorded frequency shift is shown on Fig. 23 versus the laser detuning. The shift is well-fitted by a linear function with a slope of $-26.6 \, \mathrm{mHz \, MHz^{-1}}$. Having no second similar DFB diode laser set-up, we did not measure the laser frequency stability. Taking into account that we have the same diode laser and laser frequency stabilization setup than the one reported in [35], we expect similar performances, *i.e.*, a standard deviation of $\sim 5 \, \mathrm{kHz}$ at 1000 second of averaging time. This yields a clock-fractional-frequency stability of about 1.4×10^{-14} at 1000 s.

E. f_0 vs f_m

For the sake of completeness, we have measured the clock shift versus polarization (and phase) modulation frequency f_m. Results are reported in Fig. 24. The other parameters are fixed. The shift coefficient is $3.17 \, \mathrm{mHz \, Hz^{-1}}$ at $f_m = 250 \, \mathrm{Hz}$. As f_m is synchronized to the LO, which exhibits in the worst case (unlocked) a frequency stability at the level of 7×10^{-11} at 1000 s (see Fig. 18), the effect of the polarization and phase modulation frequency on the clock shift is negligible, *i.e.* 6.0×10^{-21} at 1000 s second.

F. f_0 vs B_0

The clock frequency shift versus the magnetic field strength is shown on Fig. 25. The experimental shift
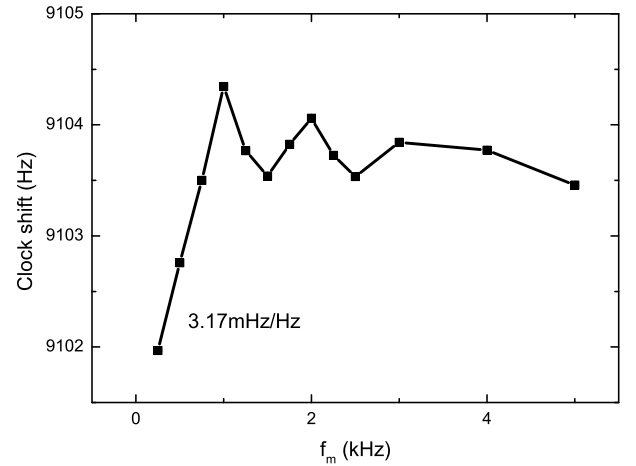

FIG. 24. (Color online) Clock frequency as function of polarization(phase) modulation frequency f_m. All other working parameters is the same as Fig. 10.

is in good agreement with the theoretical prediction of the quadratic Zeeman shift [38], $f_0 = 4.27 \times 10^{-2} B_0^2$, with B_0 in µT. In order to measure the time evolution of the magnetic field, we locked the LO frequency to the magnetic-field sensitive Zeeman CPT transition $|F=3, m_F = -1\rangle \rightarrow |F=4, m_F = -1\rangle$. The latter exhibits a sensitivity $7.01 \, \mathrm{kHz \, µT^{-1}}$. The Allan standard deviation of the Zeeman frequency (f_Z) is shown in the inset of Fig. 25. The measured frequency deviation is about $0.1 \, \mathrm{Hz}$ at 1000 s, corresponding to a magnetic field deviation of $14 \, \mathrm{pT}$ at $\tau = 1000 \, \mathrm{s}$. For a mean magnetic field of $3.43 \, \mathrm{µT}$, this yields a fractional frequency stability of 0.4×10^{-15} at 1000 s.
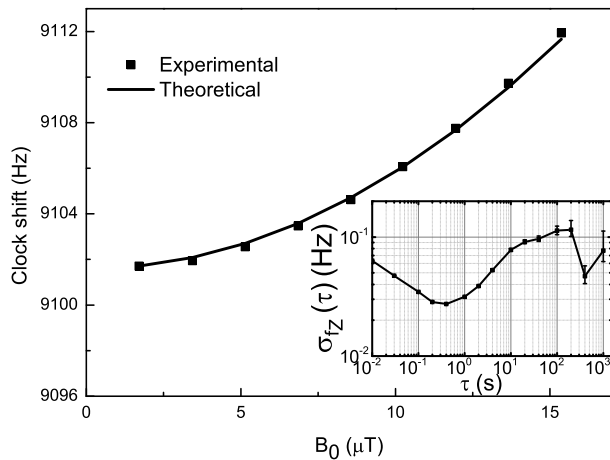
FIG. 25. (Color online) Clock frequency as function of magnetic field B_0. Inset: Allan deviation of the Zeeman frequency. All other working parameters is the same as Fig. 10.

G. Mid-term stability

With the shift coefficients and the Allan standard deviation of the involved parameters, we can estimate the various contributions to the mid-term clock frequency stability. They are listed in Table II for a $1000\,\text{s}$ averaging time. Their quadratic sum leads to a frequency stability of 4.2×10^{-13} at $\tau = 1000\,\text{s}$, in very good agreement with the measured stability 4.21×10^{-13} (see Fig. 18). Again, the main contribution to the instability comes from the microwave power fluctuations, before the laser power and frequency fluctuations. Thus in the future, it is necessary to stabilize the microwave power to improve both the short-and-mid-term frequency stability.

TABLE II. Noise contributions to the stability at $1000\,\text{s}$.

Parameter	coefficient	$\sigma_y(1000s) \times 10^{13}$
T_{cell}	$0.47\,\text{Hz}\,\text{K}^{-1}$	2.7×10^{-2}
P_L	$14.9\,\text{Hz}\,\text{mW}^{-1}$	0.26
$P_{\mu w}$	$-7.7\,\text{Hz}\,\text{dBm}^{-1}$	4.2
Δ_L	$-26.6\,\text{mHz}\,\text{MHz}^{-1}$	0.14
B_0	$0.29\,\text{Hz}\,\mu\text{T}^{-1}$	0.4×10^{-2}
Total		4.2

VI. CONCLUSIONS

We have implemented a compact vapor cell atomic clock based on the DM CPT technique. A detailed characterization of the CPT resonance versus several experimental parameters was performed. A clock frequency stability of $3.2 \times 10^{-13}\tau^{-1/2}$ up to $100\,\text{s}$ averaging time was demonstrated. For longer averaging times, the Allan deviation scales as $\sqrt{\tau}$, signature of a random walk frequency noise. It has been highlighted that the main limitation to the clock short and mid-term frequency stability is the fluctuations of the microwave power feeding the EOPM. Improvements could be achieved by implementing a microwave power stabilization. Another or complementary solution could be to choose a finely tuned laser power value minimizing the microwave power sensitivity. This adjustment could be at the expense of the signal reduction and a trade-off has to be found. Nevertheless, the recorded short-term stability is already at the level of best CPT clocks [31, 33] and close to state-of-the art Rb vapor cell frequency standards. These preliminary results show the possibility to a high-performance and compact CPT clock based on the DM-CPT technique.

[1] J. Camparo, The rubidium atomic clock and basic research, Physics Today, pp 33–39 (November 2007).
[2] S. Micalizio, C. E. Calosso, A. Godone and F. Levi, Metrological characterization of the pulsed Rb clock with optical detection, Metrologia **49**, 425-436 (2012).
[3] T. Bandi, C. Affolderbach, C. Stefanucci, F. Merli, A. K. Skrivervik and G. Mileti, coninuous-wave double-resonance rubidium standard with $1.4 \times 10^{-13}\tau^{-1/2}$ sta-

bility, IEEE Ultrason. Ferroelec. Freq. Contr. **61**, 11, 1769–1778 (2014).
[4] S. Kang, M. Gharavipour, C. Affolderbach, F. Gruet, and G. Mileti, Demonstration of a high-performance pulsed optically pumped Rb clock based on a compact magnetron-type microwave cavity, J. Appl. Phys. **117**, 104510 (2015).
[5] A. Godone, F. Levi, C. E. Calosso and S. Micalizio,

High-performing vapor cell frequency standards, Rivista di Nuovo Cimento **38**, 133-171 (2015).

[6] G. Alzetta, A. Gozzini, L. Moi, and G. Orriols, An experimental method for the observation of R. F. transitions and laser beat resonances in oriented Na vapour, Il Nuovo Cimento **36 B**, 5 (1976).

[7] E. Arimondo, Coherent population trapping in laser spectroscopy, Progress in Optics **35**, 257-354 (1996).

[8] K. Bergmann, H. Theuer, and B. W. Shore, Coherent population transfer among quantum states of atoms and molecules. Rev. Mod. Phys., **70**, 1003-1025 (1998).

[9] R. Wynands and A. Nagel, Precision spectroscopy with coherent dark states, Appl. Phys. **B 68**, 1 (1999).

[10] J. Vanier, Atomic clocks based on coherent population trapping: A review, Appl. Phys. B **81**, 421-442 (2005).

[11] M. Bajcsy, A. S. Zibrov and M. D. Lukin, Stationary pulses of light in an atomic medium, Nature **426,** 638-641 (2003).

[12] P. D. D. Schwindt, S. Knappe, V. Shah, L. Hollberg, J. Kitching, L. A. Liew and J. Moreland, Chip-scale atomic magnetometer, Appl. Phys. Lett. **85,** 26, 6409-6411 (2004).

[13] E. Breschi, Z. D. Gruji, P. Knowles and A. Weis, A high-sensitivity push-pull magnetometer, Appl. Phys. Lett. **104,** 023501 (2014).

[14] A. Aspect, E. Arimondo, R. Kaizer, N. Vansteenkiste and C. Cohen-Tannoudji, Transient velocity-selective coherent population trapping in one dimension, J. Opt. Soc. Am. B **6**, 2112-2124 (1989).

[15] J. Vanier and C. Mandache, The passive optically pumped Rb frequency standard: The laser approach, Appl. Phys. B Lasers Opt. **87**, 565-593 (2007).

[16] J. E. Thomas, S. Ezekiel, C. C. Leiby, R. H. Picard, and C. R. Willis, Ultrahigh-resolution spectroscopy and frequency standards in the microwave and far-infrared regions using optical lasers, Opt. Lett. **6**, 298-300 (1981).

[17] J. E. Thomas, P. R.Hemmer, S. Ezekiel, C. C. Leiby,, R. H. Picard, and C. R. Willis, Observation of Ramsey fringes using a stimulated, resonance Raman transition in a sodium atomic beam, Phys. Rev. Lett. **48**, 867-870 (1982).

[18] N. Cyr, M. Tetu, and M. Breton, All-optical microwave frequency standard - a proposal, IEEE Trans. Instrum. Measur. **42**, 640-649 (1993).

[19] J. Kitching, N. Vukicevic, L. Hollberg, S. Knappe, R.Wynands, and W. Weidemann, A microwave frequency reference based on VCSEL-driven dark line resonances in Cs vapor, IEEE Trans. Instrum. Measur. **49**, 1313-1317 (2000).

[20] J. Kitching, L. Hollberg, S. Knappe, and R. Wynands, Compact atomic clock based on coherent population trapping, Electron. Lett. **37**, 1449 (2001).

[21] J. Kitching, S. Knappe, and L. Hollberg, Miniature vapor-cell atomic-frequency references, Appl. Phys. Lett. **81**, 553 (2002).

[22] L. Liew, S. Knappe, J. Moreland, H. Robinson, L. Hollberg, and J. Kitching, Microfabricated alkali atom vapor cells, Appl. Phys. Lett. **84**, 2694 (2004).

[23] S. Knappe, V. Shah, P. D. D. Schwindt, L. Hollberg, J. Kitching, L.-A.Liew, and J. Moreland, A microfabricated atomic clock, Appl. Phys. Lett. **85**, 1460 (2004).

[24] http://www.microsemi.com/products/timing-synchronizationsystems/embedded-timing-solutions/components/sa-45s-chip-scale-atomic-clock#resources

[25] http://www.inrim.it/Mclocks

[26] V. Shah and J. Kitching, Advances in coherent population trapping for atomic clocks, in Advances in Atomic, Molecular,and Optical Physics, edited by E. Arimondo, P. R. Berman, and C. C. Lin, Vol. 59 (Elsevier, Amsterdam, 2010).

[27] Peter Yun, Doctor thesis, Exploring New Approaches to Coherent Population Trapping Atomic Frequency Standards, Wuhan Institute of Physics and Mathematics Chinese Academy of Sciences, Wuhan, China, 2012.

[28] P. Yun, J.-M. Danet, D. Holleville, E. de Clercq, and S. Guérandel, Constructive polarization modulation for coherent population trapping clock, Appl. Phys. Lett. **105**, 231106 (2014).

[29] Y.-Y. Jau, E. Miron, A. B. Post, N. N. Kuzma, and W. Happer, Push-Pull Optical Pumping of Pure Superposition States, Phys. Rev. Lett. **93**, 160802-1-4 (2004).

[30] X. Liu, J.-M. Mérolla, S. Guérandel, C. Gorecki, E. de Clercq, and R. Boudot, Coherent population trapping resonances in buffer-gas-filled Cs-vapor cells with push-pull optical pumping, Phys. Rev. A **87**, 013416 (2013).

[31] M. Abdel Hafiz and R. Boudot, A coherent population trapping Cs vapor cell atomic clock based on push-pull optical pumping, J. Appl. Phys. **118**, 124903 (2015).

[32] T. Zanon, S. Guérandel, E. de Clercq, D. Holleville, N. Dimarcq and A. Clairon, High Contrast Ramsey Fringes with Coherent-Population-Trapping Pulses in a Double Lambda Atomic System, Phys. Rev. Lett. **94,** 193002 (2005).

[33] J.-M. Danet, O. Kozlova, P. Yun, S. Guérandel and E. de Clercq, Compact atomic clock prototype based on coherent population trapping, EPJ Web of Conferences **77**, 00017 (2014).

[34] R.Schmeissner, N. von Bande , A.Douahi, O.Parillaud, M.Garcia, M.Krakowski, M.Baldy, The optical feedback spatial phase driving perturbations of DFB laser diodes in an optical clock, Proceedings of the 2016 European Frequency and Time Forum, York (2016), available at http://www.eftf.org/previousmeetings.php.

[35] M. Abdel Hafiz, G. Coget, E. De Clercq, R. Boudot, Doppler-free spectroscopy on the Cs D1 line with a dual-frequency laser, Opt. Lett. **41**, 2982-2985 (2016).

[36] B. François, C. E. Calosso, M. Abdel Hafiz, S. Micalizio, and R. Boudot, Simple-design ultra-low phase noise microwave frequency synthesizers for high-performing Cs and Rb vapor-cell atomic clocks, Rev. Sci. Instrum. **86**, 094707 (2015).

[37] C. E. Calosso, S. Micalizio, A. Godone, E. K. Bertacco, F. Levi. Electronics for the pulsed rubidium clock: Design and characterization. IEEE Trans. Ultrason. Ferroelectr. Freq. Control **54**, 1731-1740 (2007).

[38] J. Vanier and C. Audoin, *The quantum physics of atomic frequency standards* (Adam Hilger, Bristol, 1989).

[39] A. Godone, F. Levi, S. Micalizio, and J. Vanier, Dark-line in opticall-thic vapors: inversion phenomena and line width narrowing, Eur. Phys. J. D **18**, 5-13 (2002).

[40] P. Yun, S. Guérandel, and E. de Clercq , Coherent population trapping with polarization modulation, J. Appl. Phys. 119, 244502 (2016).

[41] P. Yun, S. Mejri, F. Tricot, M. Abdel Hafiz, R. Boudot, E. de Clercq, S. Guérandel, Double-modulation CPT cesium compact clock, 8th Symposium on Frequency Standards and Metrology 2015, J. of Physics: Conference Series **723**, 012012 (2016).

[42] Enrico Rubiola, Phase noise and frequency stability in oscillators, Cambridge University Press, 2009.

[43] C. Audoin, V. Candelier, and N. Dimarcq, A limit to the frequency stability of passive frequency standards due to an intermodulation effect, IEEE Trans. Instrum. Meas. **40**, 121 (1991).

[44] O. Kozlova, S. Guérandel, and E. de Clercq, Temperature and pressure shift of the Cs clock transition in the presence of buffer gases: Ne, N_2, Ar, Phys. Rev. A **83**, 062714 (2011).

[45] O. Kozlova, J-M. Danet, S. Guérandel, and E. de Clercq, Limitations of long-term stability in a coherent population trapping Cs Clock, IEEE Trans. Instrum. Meas. **63**, 1863 (2014).

[46] F. Levi, A. Godone, J. Vanier, The light-shift effect in the coherent population trapping cesium maser, IEEE Trans. Ultrason. Ferroelectr. Freq. Control **47**, 466 (2000).

[47] M. Zhu and L.S. Cutler, Theoretical and experimental study of light shift in a CPT-based Rb vapor cell frequency standard, in Proceedings of the 32nd Precise Time and Time Interval Systems and Applications Meeting, p. 311, ed. by L.A. Breakiron (US Naval Observatory, Washington, DC, 2000).

[48] C. Affolderbach, C. Andreeva, S. Cartaleva, T. Karaulanov, G. Mileti, and D. Slavov, Light-shift suppression in laser optically pumped vapour-cell atomic frequency standards, Appl. Phys. B **80**, 841-8 (2005).

[49] V. Shah, V. Gerginov, P. D. D. Schwindt, S. Knappe, L. Hollberg and J. Kitching, Continuous light- shift correction in modulated coherent population trapping clocks, Appl. Phys. Lett. **89,** 151124 (2006).

[50] B. H. McGuyer, Y. Y. Jau and W. Happer, Simple method of light-shift suppression in optical pumping systems, Appl. Phys. Lett. **94**, 251110 (2009).